



Capsicumicine, a New Bioinspired Peptide from Red Peppers Prevents Staphylococcal Biofilm *In Vitro* and *In Vivo* via a Matrix Anti-Assembly Mechanism of Action

✉ Rafael Gomes Von Borowski,^{a,b} Sophie Chat,^a Rafael Schneider,^{a,b} Sylvie Nonin-Lecomte,^c Serge Bouaziz,^c Emmanuel Giudice,^a Aline Rigon Zimmer,^b Simone Cristina Baggio Gnoatto,^b Alexandre José Macedo,^{b,d} ✉ Reynald Gillet^a

^aUniversité de Rennes, CNRS, Institut de Génétique et de Développement de Rennes (IGDR), UMR6290, Rennes, France

^bPrograma de Pós-Graduação em Ciências Farmacêuticas, Faculdade de Farmácia, Universidade Federal do Rio Grande do Sul, Porto Alegre, Brazil

^cUniversité de Paris, CNRS, CiTCoM (Cibles Thérapeutiques et Conception de Médicaments) UMR 8038, Faculté de Pharmacie, Paris, France

^dCentro de Biotecnologia da Universidade Federal do Rio Grande do Sul, Porto Alegre, Brazil

ABSTRACT Staphylococci are pathogenic biofilm-forming bacteria and a source of multidrug resistance and/or tolerance causing a broad spectrum of infections. These bacteria are enclosed in a matrix that allows them to colonize medical devices, such as catheters and tissues, and that protects against antibiotics and immune systems. Advances in antibiofilm strategies for targeting this matrix are therefore extremely relevant. Here, we describe the development of the *Capsicum* pepper bioinspired peptide “capsicumicine.” By using microbiological, microscopic, and nuclear magnetic resonance (NMR) approaches, we demonstrate that capsicumicine strongly prevents methicillin-resistant *Staphylococcus epidermidis* biofilm via an extracellular “matrix anti-assembly” mechanism of action. The results were confirmed *in vivo* in a translational preclinical model that mimics medical device-related infection. Since capsicumicine is not cytotoxic, it is a promising candidate for complementary treatment of infectious diseases.

IMPORTANCE Pathogenic biofilms are a global health care concern, as they can cause extensive antibiotic resistance, morbidity, mortality, and thereby substantial economic loss. So far, no effective treatments targeting the bacteria in biofilms have been developed. Plants are constantly attacked by a wide range of pathogens and have protective factors, such as peptides, to defend themselves. These peptides are common components in *Capsicum baccatum* (red pepper). Here, we provide insights into an antibiofilm strategy based on the development of capsicumicine, a natural peptide that strongly controls biofilm formation by *Staphylococcus epidermidis*, the most prevalent pathogen in device-related infections.

KEYWORDS antibiofilm, biofilm, matrix, peptides, anti-assembly, resistance, tolerance, *Staphylococcus*, antimicrobial peptides

Antimicrobial failure is a worldwide challenge, currently addressed by a WHO global action plan (1). A lack of new antibiotics and the inappropriate use of older treatments mean that multidrug-resistant strains are increasing (2). This process is favored by biofilm development, and microorganisms enclosed in biofilm matrices have antibiotic resistance that is up to 1,000 times higher than that of planktonic ones (3). This makes the matrix itself an important target for biofilm control. Biofilms are organized microbial clusters made of a self-assembled matrix that usually attaches to a surface, whether abiotic (medical devices such as catheters, teeth, etc.) or biotic (host tissues, mucus, chronic wounds, etc.) (4, 5). Since the bacteria are embedded into this matrix, they are harder to treat because of their increased tolerance and resistance to antibiotics, disinfectants, and host defenses (6, 7). Other advantages over planktonic forms

Citation Gomes Von Borowski R, Chat S, Schneider R, Nonin-Lecomte S, Bouaziz S, Giudice E, Rigon Zimmer A, Baggio Gnoatto SC, Macedo AJ, Gillet R. 2021. Capsicumicine, a new bioinspired peptide from red peppers prevents staphylococcal biofilm *in vitro* and *in vivo* via a matrix anti-assembly mechanism of action. *Microbiol Spectr* 9:e00471-21. <https://doi.org/10.1128/Spectrum.00471-21>.

Editor Aude A. Ferran, INHERES

Copyright © 2021 Gomes Von Borowski et al. This is an open-access article distributed under the terms of the [Creative Commons Attribution 4.0 International license](https://creativecommons.org/licenses/by/4.0/).

Address correspondence to Alexandre José Macedo, alexandre.jose.macedo@gmail.com, or Reynald Gillet, reynald.gillet@univ-rennes1.fr.

Received 20 July 2021

Accepted 9 September 2021

Published 27 October 2021

include physiological and biochemical changes, beneficial quorum sensing, higher (up to 100 times) mutation rates, and persister cell development (8–10). Staphylococci are the most frequent sources of nosocomial infections, particularly *Staphylococcus epidermidis* and *Staphylococcus aureus*. While *S. aureus* expresses many virulence factors such as toxins and proteases, for *S. epidermidis*, the formation of biofilm is the most important mechanism in infection development (11). *Staphylococcus epidermidis* is the most frequent coagulase-negative staphylococcal (CoNS) infection-causing disease (12), surviving on various surfaces for months (13). It is present in 30% of health care-involved bloodstream infections and is significantly associated with medical device infections, including 15 to 40% of prosthetic valve endocarditis (14) and 30 to 43% of prosthetic orthopedic device infections (15). More than 150 million intravascular catheters are used per year in the United States, and there are about 250,000 catheter-related infections (16, 17). These bacteria are developing antibiotic multiresistances, such as elevated glycopeptide MICs (18), and 73 to 88% of isolates display resistance to oxacillin, fluoroquinolones, macrolides, clindamycin, and trimethoprim-sulfamethoxazole (19–21).

In this circumstance, the extracellular matrix is a complex physicochemical barrier representing one of the biggest challenges in microbial treatments (4). Therefore, the development of antivirulence strategies, such as antibiofilm agents, is crucial for the current antibiotic crisis, and peptides are an increasing arsenal for controlling pathogenic biofilms (22–24). Here, we describe the discovery of the antibiofilm peptide capsicumicine, inspired by natural peptides from the seeds of the red pepper *Capsicum baccatum*. Our data suggest that capsicumicine is a nonantibiotic peptide displaying a matrix anti-assembly (MAA) mechanism of action by interfering with polysaccharides. Notably, we report an *in vivo* anti-infective proof of concept toward the use of capsicumicine for complementary treatment of infectious diseases.

RESULTS

Capsicumicine prevents biofilm formation without antibiotic activity. We synthesized the following three peptides inspired by a natural antibiofilm fraction previously identified from *Capsicum baccatum* var. *pendulum* pepper seeds (25): P1 (RVQSEEGEDQISQRE), P2 (RAEAFQTAQALPGLCRI), and P3 (RSCQQIQQAAQLSSCQQYLKQ). To find the most active one, we exposed these compounds to strong biofilm-forming *S. epidermidis* RP62A (ATCC 35984). After 24 h, crystal violet was used to quantify the remaining biofilm (Fig. 1A). P3, named “capsicumicine,” was the most active with particularly strong antibiofilm activity. Biofilm decreases were observed at all tested concentrations but especially at 10 μ M. There, biofilm was reduced by over 91%, independently of cell growth inhibition (Fig. 1B). To examine the effects of capsicumicine on growth, we checked *S. epidermidis* CFU counts after peptide exposure. As expected, the CFU were unchanged by capsicumicine, so the peptide’s biofilm inhibition is not due to bactericidal activity (Fig. 1B). To verify the interactions between capsicumicine and established biofilm, we exposed a preexisting *S. epidermidis* biofilm to a single concentration (100 μ M) of the peptide. At that concentration, capsicumicine accounts for 15% of the disruption of preexisting biofilm (see Fig. S1 in the supplemental material). To study the peptide’s possible mechanisms of action, we selected several genes involved in different stages of biofilm development (*atIE*, *aap*, *agrC*, *icaA*, *leuA*, *saeR*, *saeS*, and *sarA*); primers are listed in Table S1 in the supplemental material. Fold changes were analyzed by quantitative real-time PCR (qRT-PCR). Since exposed bacteria remain planktonic, we compared their relative gene expressions to planktonic control cells. For all tested genes, capsicumicine-exposed cells show the same fold changes as the control (Fig. 1C).

Capsicumicine is not cytotoxic in mammalian cells. To ensure that capsicumicine is safe before propose *in vivo* trials, we verified its cytotoxicity in seven different representative human cell lines. We used automated image-based cellular content analysis and found that capsicumicine-treated cells perform exactly the same as untreated controls, displaying no cytotoxicity (Fig. 1D).

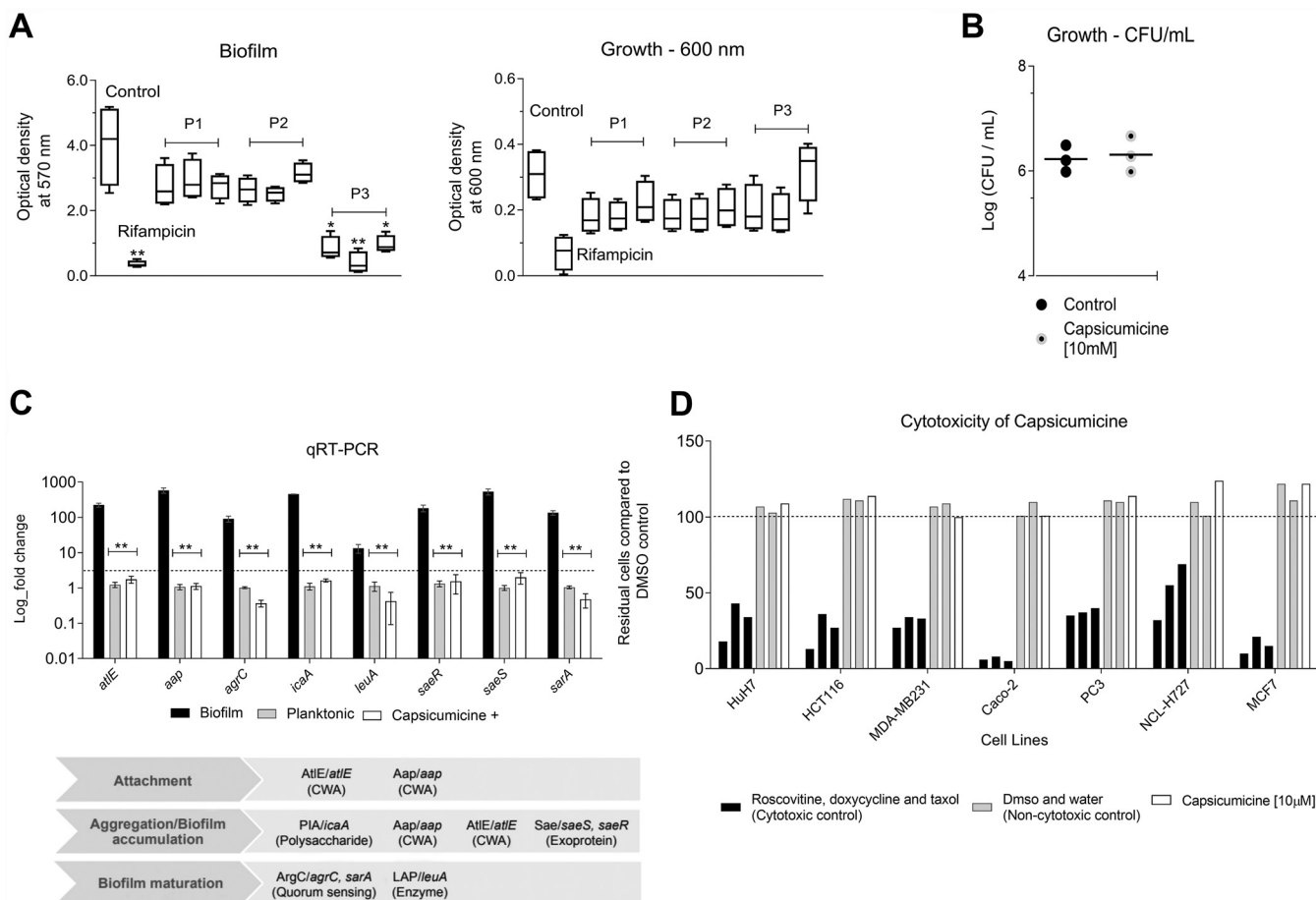


FIG 1 Antibiofilm activity of bioinspired peptides and cytotoxicity. (A) Antibiofilm activity of peptides P1, P2, and P3 (capsicumine) at 1, 10, and 100 μ M. Quantification of *Staphylococcus epidermidis* (ATCC 35984) biofilm and growth were done at an optical density of 570 (crystal violet) and 600 nm (without crystal violet), respectively, bacteria without peptide exposure (control) and the antibiotic control, 16 μ g/ml rifampin. Student's *t* test, *, $P \leq 0.05$; **, $P \leq 0.01$. (B) Growth of bacteria at 10 μ M using CFU. (C) Gene expression (mean log fold changes \pm standard errors of the mean) of the encoding genes involved in *S. epidermidis* biofilm formation compared to the planktonic (gray) and biofilm controls (black) with the *sarA* gene used as a reference. The group exposed to capsicumine is shown in white. CWA, cell wall-anchored proteins. Two-way analysis of variance (ANOVA) and Tukey's multiple-comparison test, **, $P \leq 0.0015$. (D) Capsicumine cytotoxicity evaluation in representative human cell lines shown via automated image-based cellular content analysis. HuH7, hepatocellular carcinoma; Caco-2, colorectal adenocarcinoma; MDA-MB231, breast adenocarcinoma; HCT116, colorectal carcinoma; PC3, prostatic adenocarcinoma; NCL-H727, lung carcinoma; MCF7, breast cancer. Cell counts are presented as residual cell percentages (%) compared to the average of the DMSO control, with water control also shown (gray bars). The black bars on the left show cytotoxic controls (roscovitine, doxycycline, and taxol), while the white bars are cells exposed to 10 μ M capsicumine.

Independently of cell interactions, capsicumine impairs biofilm attachment, aggregation, and accumulation.

To explore its activity during the first stages of biofilm development, we analyzed biofilm cultures on polystyrene coupons with and without capsicumine after 1, 4, and 24 h. Scanning electron microscopy (SEM) analysis shows that bacterial attachment decreases after 1 h of capsicumine exposure, with biofilm accumulation and cell aggregation profiles strongly reduced after 4 and 24 h (Fig. 2A). This demonstrates that capsicumine prevents *S. epidermidis* coupon adhesion, and notably this activity still occurs after 24 h of incubation. In order to localize the peptide, we used capsicumine conjugated to fluorescein isothiocyanate (capsicumine-FITC) and confocal fluorescence microscopy (CFM). Analysis of the CFM images showed that capsicumine-FITC stays associated with extracellular components, not entering into bacterial cells or the walls or membranes (Fig. 2B).

Capsicumine disturbs *S. epidermidis* matrix assembly. Since capsicumine's antibiofilm activity was not associated with direct bacterial interactions or gene expression modulation, we used various microscopic approaches to investigate the interactions between the peptide and the extracellular matrix. In the biofilm control, macroscopic observation shows a homogenous whitish adhered layer covering the walls and

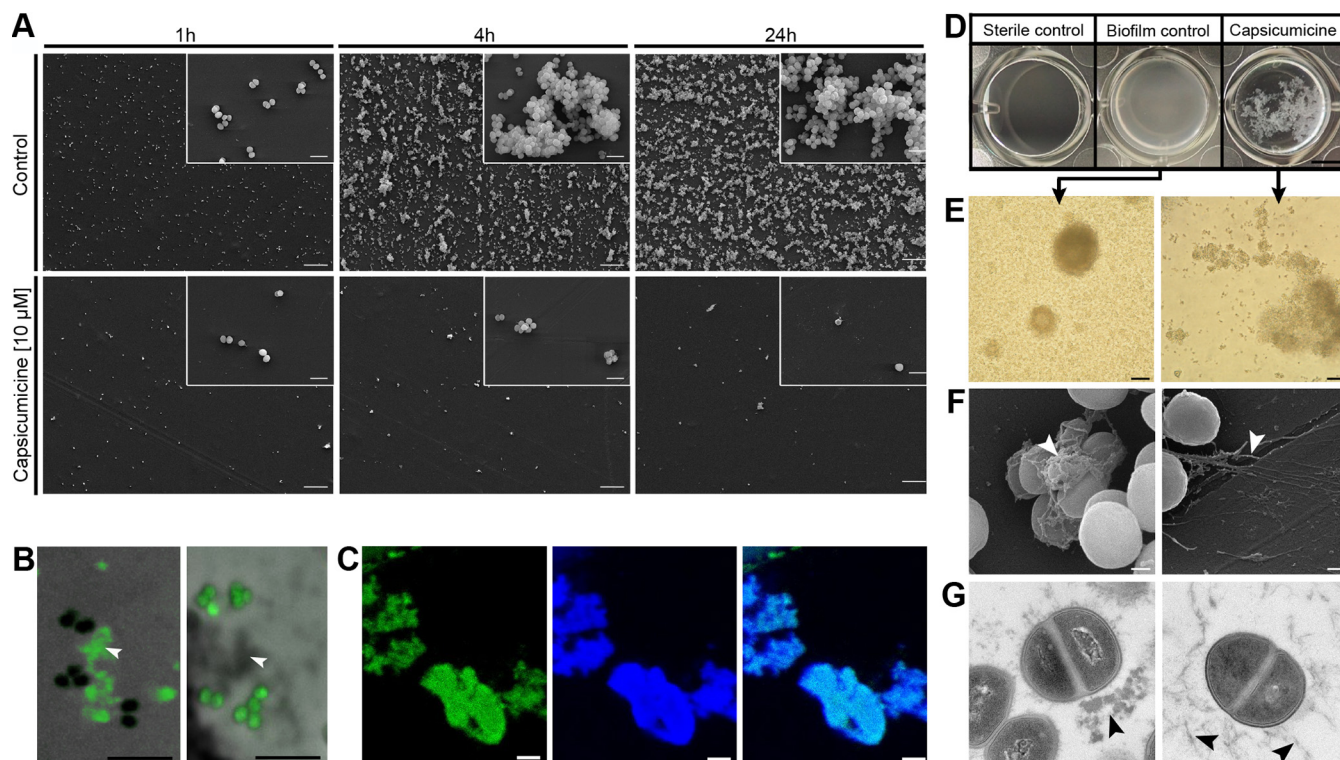


FIG 2 Biological characterization of capsicumicine by microscopic approaches. (A) SEM images of polystyrene coupons after 1, 4, or 24 h of culture with *Staphylococcus epidermidis* (ATCC 35984). (Top) Peptide-less biofilm control. (Bottom) Cultures exposed to 10 μM capsicumicine. Magnification $\times 500$, with insets at $\times 5,000$; scale bars, 10 μm . (B) CFM images. (Left) *S. epidermidis* after exposure to 10 μM capsicumicine-FITC with the peptide in green (fluorescence) and the bacterial cells in black (no fluorescence). (Right) Control, *S. epidermidis* after exposition to pseudonajide-FITC, an antibacterial peptide, this time showing the extracellular components in gray (no fluorescence). White arrows indicate extracellular content. Scale bars, 5 μm . (C) CFM images. *S. epidermidis* after exposure to 10 μM capsicumicine-FITC (left) and after exposure to concanavalin A conjugates (selectively reveals saccharides) (center) and their colocalization (right). Scale bars, 5 μm . (D to G) The organizational state of *S. epidermidis* biofilm after 24 h in the presence (right) or absence (control, left) of capsicumicine. (D) Macroscopic examination by pictures from the bottom of 24-well plates. The “sterile control” shows no bacteria or biofilm formation, the “biofilm control” shows homogenous adhered layers of bacteria, and “capsicumicine” shows nonadhered bacteria but agglutinates. Scale bar, 5 mm. (E) TLM images show the biofilm control with overlapping attached bacterial clusters, while the capsicumicine-exposed culture shows agglutinated nonadhered cells. Scale bar, 20 μm . (F) SEM images show the control with dense globular-like matrix features, while the capsicumicine-exposed culture shows fibrillary branch-like oligomer structures. Scale bar, 200 nm. (G) TEM images of the biofilm control show denser assembled structures, while the capsicumicine-exposed displays thin fibrillary oligomer structures. Scale bar, 200 nm. Arrows indicate the matrices.

bottoms of the well (Fig. 2D, middle), but when capsicumicine is present, we see whitish flocculent nonadhered heterogeneous agglutinates (Fig. 2D, right). Transmitted light microscopy (TLM) images match with these macroscopic observations (Fig. 2E). Crucially, SEM and transmission electron microscopy (TEM) techniques yield ultrastructural descriptions that support these results, with the control biofilm matrix showing denser assembled globular-like structures, while the capsicumicine-exposed matrix is less dense and has thin fibrillary branch-like structures (Fig. 2F and G). However, cellular morphologies are not different from the controls. Therefore, different imaging techniques prove that matrix assembly changes when capsicumicine is present.

Capsicumicine interacts with matrix polysaccharides. To explore the peptide’s affinity with these major matrix components, we exposed *S. epidermidis* cultures to capsicumicine (-FITC; green) and saccharide staining, and then analyzed them all by CFM. We used concanavalin A and calcofluor to selectively target matrix saccharides (blue). Amounts of capsicumicine-FITC appear exclusively on the matrix (Fig. 2B left; see also Fig. S2B in the supplemental material), and its colocalization indicates the interaction between both marked elements (Fig. 2C, right; see also Fig. S2A). Visualization was done by individual (Fig. 2C, left and center) and colocalization fluorescence (Fig. 2C, right). The peptide control was pseudonajide-FITC, an antibacterial peptide; it showed green fluorescence in the cells but not in the matrix (Fig. 2B right; see also Fig. S2C). To explore whether capsicumicine features are compatible with carbohydrate-binding modules (CBMs), we performed

a BLAST and amino acid alignments between capsicumicine and chitin-, chitosan-, and polysaccharide intercellular adhesin (PIA)-binding proteins (see Table S2 in the supplemental material). UniProt tools (26) and CAZy information crossing (27) showed that capsicumicine does in fact present CBM homology with all tested proteins (see Fig. S3 in the supplemental material).

Capsicumicine shifts staphylococcal synthetic matrix. To confirm these interactions in the absence of bacteria metabolic or regulatory influences, we adapted a model of artificial staphylococcal biofilm assembly to test it. For this purpose, we used chitosan in order to mimic natural poly-*N*-acetylglucosamine (PNAG) biofilm. Briefly, we monitored the real-time molecular self-assembly (RTMSA) reaction (based on the assembly reaction of the synthetic staphylococcal matrix; see Materials and Methods) by measuring the optical density at 600 nm (OD_{600}) as a function of time with or without capsicumicine. OD increases when capsicumicine is present, which shows that the molecular self-assembly reaction is quicker overall (Fig. 3A). The profiles of assembled matrices are visually different, with larger agglutinates in the presence of capsicumicine, although both controls are similar (Fig. 3A). Remarkably, these profiles are comparable to those previously observed in the presence of bacteria (Fig. 2D). To evidence the interactions between capsicumicine and target saccharides, we performed nuclear magnetic resonance (NMR) titration experiments using chitosan as a mimic of the matrix PNAG. The evolutions of the capsicumicine NMR spectra upon chitosan addition were monitored. Reference one-dimensional (1D) proton NMR spectra were recorded at all tested conditions. Chitosan was gradually added from a concentrated solution, and spectra changes were monitored. This solution remained clear during the 7 days of recording. The addition of soluble chitosan drives noticeable changes of the resonance frequency of some of the amide protons mainly in the N-terminal part of the peptide (S2, C3, Q4, and R1 [not shown]) (Fig. 3B). Conversely, to Y19, L20, and K21 NH and the Y19 aromatic proton resonances, between 6.8 and 7.2 are not sensitive to the presence of chitosan (Fig. 3E). The concentration variation of chitosan was estimated to be less than 0.5 eq at the end of the titration. This small quantity of chitosan drives spectral modifications in the N-terminal part of capsicumicine and strongly supports the interaction between both partners. The important broadening observed after 1 day shows that the peptide structure keeps evolving over time and that this is not due to cysteine oxidation (Fig. 4D and E). These experiments were repeated, adding gelled chitosan instead of soluble chitosan, mimicking an assembled matrix. It does not drive any significant spectral changes except for a general line broadening, which probably arises from an increased viscosity of the solution (Fig. 3C). The sudden addition of gelled chitosan pellets in the NMR solution does not modify the spectrum either (Fig. 3D).

Structural requirements toward molecular interactions with target saccharides.

To better understand the mechanisms involved in capsicumicine bioactivity, we step toward the knowledge of its conformation in solution and molecular interactions with matrix representative saccharides. To monitor the conformation of free capsicumicine in response to time and temperature, we first used circular dichroism (CD) and nuclear magnetic resonance (NMR) spectroscopies. Spectral deconvolution using the CDSSTR algorithm discloses a helical structure (about 43 to 44%) with a nonnegligible proportion of β strands (31 to 33%) and unfolded conformations (about 20%) (see Table S3 in the supplemental material). The structure stability was assessed over 5 days, recording the CD spectra at 5°C (Fig. 4A). The main structure observed over the first 24 h is helical. After 5 days, deconvolutions show a slight decrease in the helical content. Furthermore, on the fifth day, CD spectra were also recorded at 15 and 30°C (Fig. 4B). The helical content decreases to 18 to 23%, while the β strand and turn mean proportions rose around 37% and 23%, respectively. The proportion of unfolded structures also increased. After 2 days at room temperature, a new CD spectrum was recorded at 30°C. The helix proportion became less than 15% in favor of β strand and unfolded conformations (respectively, 38 to 41% and 31 to 35%). During these days, the peptide solution remained clear, showing no macroscopic signs of aggregation. The 1D and two-dimensional (2D) NMR spectra of a 0.3 mM freshly prepared solution of

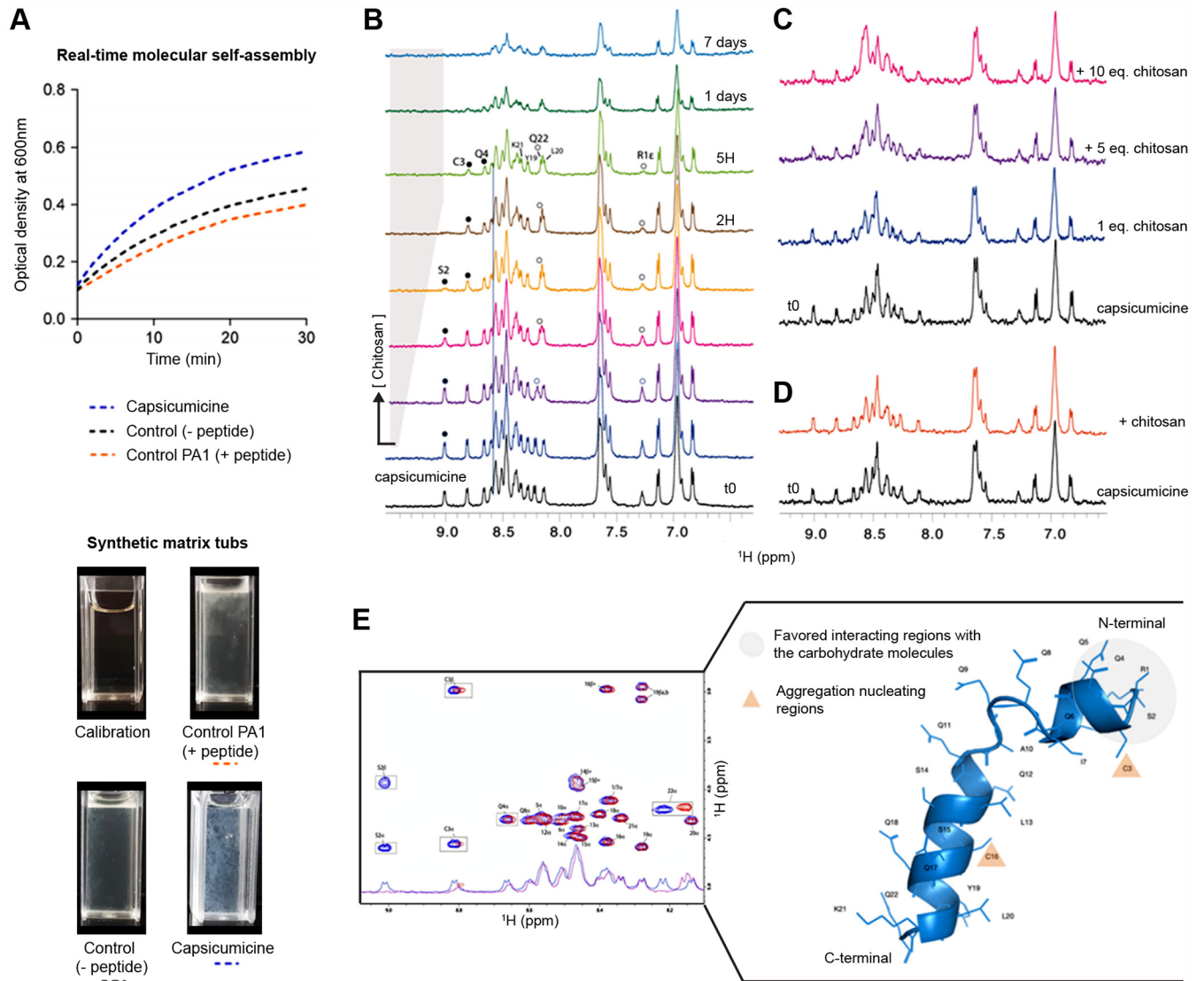


FIG 3 Molecular interactions between capsicumicine and target-saccharides. (A) RTMSA curves of artificial staphylococcal biofilm assembly. Optical densities (OD_{600}) were recorded as a function of the time in the presence of capsicumicine (blue dots) or PA1 as peptide control (orange dots) and the synthetic matrix without peptides (black dots); each reaction tub is shown under the graph. (B-D) NMR titration of capsicumicine by chitosan at 600 MHz, 10°C. (B) From the bottom to the top: increasing concentrations of soluble chitosan [<0.5 eq. and 8% of volume variation] were gradually added to capsicumicine water solution. Specific line broadenings and frequency shifts are shown in the NMR spectrum for some amide protons upon titration; white bullets for terminal R1 and Q22 and black bullets for S2, C3 and Q4. (C) Assembled chitosan gradually added to soluble capsicumicine [0.5 eq.]; an overall line broadening was observed. (D) Assembled chitosan suddenly added to soluble capsicumicine [0.5 eq.]; the orange spectrum was recorded after few minutes of stirring. (E) Superposition of capsicumicine 1D NMR and TOCSY spectra immediately after sample preparation (blue) and chitosan [10 eq.] addition (red) and; capsicumicine structure predicted by Phyre2 server; according to NMR results the aggregation nucleating regions are shown as orange triangles and favored interacting region with sugar moieties is shown in gray.

capsicumicine were recorded at 10°C, pH 5.0. All amide resonances were unambiguously assigned using total correlation spectroscopy (TOCSY) and nuclear Overhauser effect spectroscopy (NOESY) spectra, except for Q9 and Q11 residues (see Fig. S4 in the supplemental material). The spectral dispersion and the spreading of the amide proton resonances disclose that the peptide is folded with one conformation in these conditions. In accordance with CD spectra, a second set of NH resonances appears as a function of time (Fig. 4C and D), revealing conformational changes in the slow exchange regime on the NMR time scale. After 5 days, the most important chemical shift perturbations (CSP) observed on the TOCSY spectrum are clustered around the two cysteines apart from the two terminal residues (boxed cross-peaks) (Fig. 4E). Interestingly, 17 located one helix turn apart from C3 is among the most sensitive

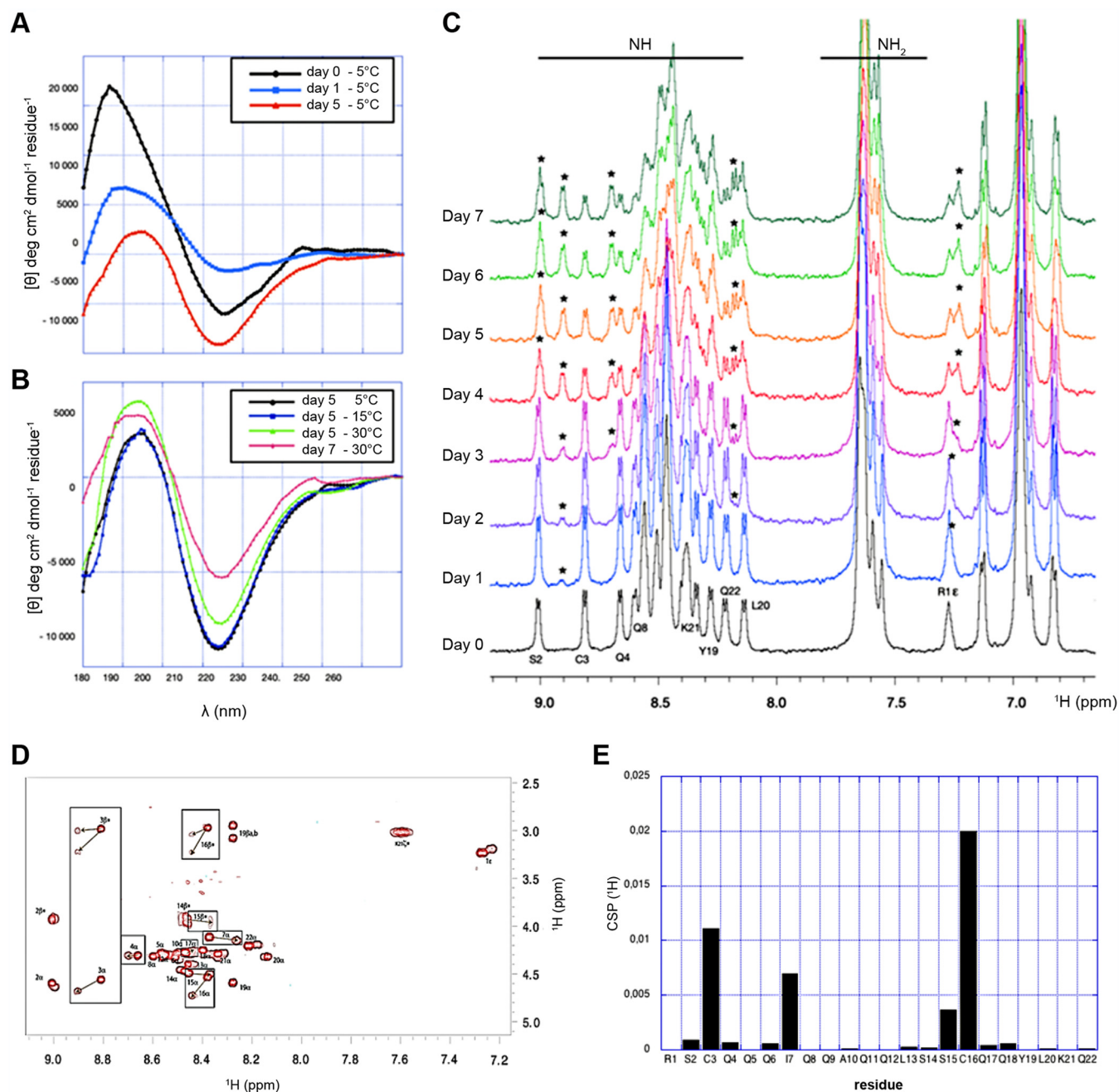


FIG 4 Capsicum conformational changes. CD spectra. (A) Evolution at 5°C over 5 days. (B) Evolution versus time and temperature. (C) NMR spectra recorded at pH 5.0, 0.3 mM, and 10°C immediately after extemporaneous preparation (bottom); a second conformation appears over the time corresponding to the second set of amide resonances (stars). (D) Superposition of capsicum TOSY spectra immediately after sample preparation (red) and at day 5 (brown). The most important chemical shift perturbations (CSP) between the original and the new conformations are boxed and clustered around the two cysteines. (E) Proton chemical shift perturbations computed from the TOSY spectra are displayed in the box.

residues to the conformational perturbation. This is due to a disulfide bridge (DB), since no reducing agent was added. Consequently, large proton chemical shift perturbations would be expected for every –NH amino acid, and this was not detected (Fig. 4D and E). The prevalence of the second conformation reaches more than 50% after 7 days (Fig. 4C, top). The solution remained clear over all of the spectra recording time.

Capsicum attenuates the dynamics of *S. aureus* (Xen36) infection on a central venous catheter. We performed a translational proof of concept evaluating long-term bacterial biofilm and related infection in mice implanted with capsicum pre-coated central venous catheter (CVC). These CVCs were previously coated using an

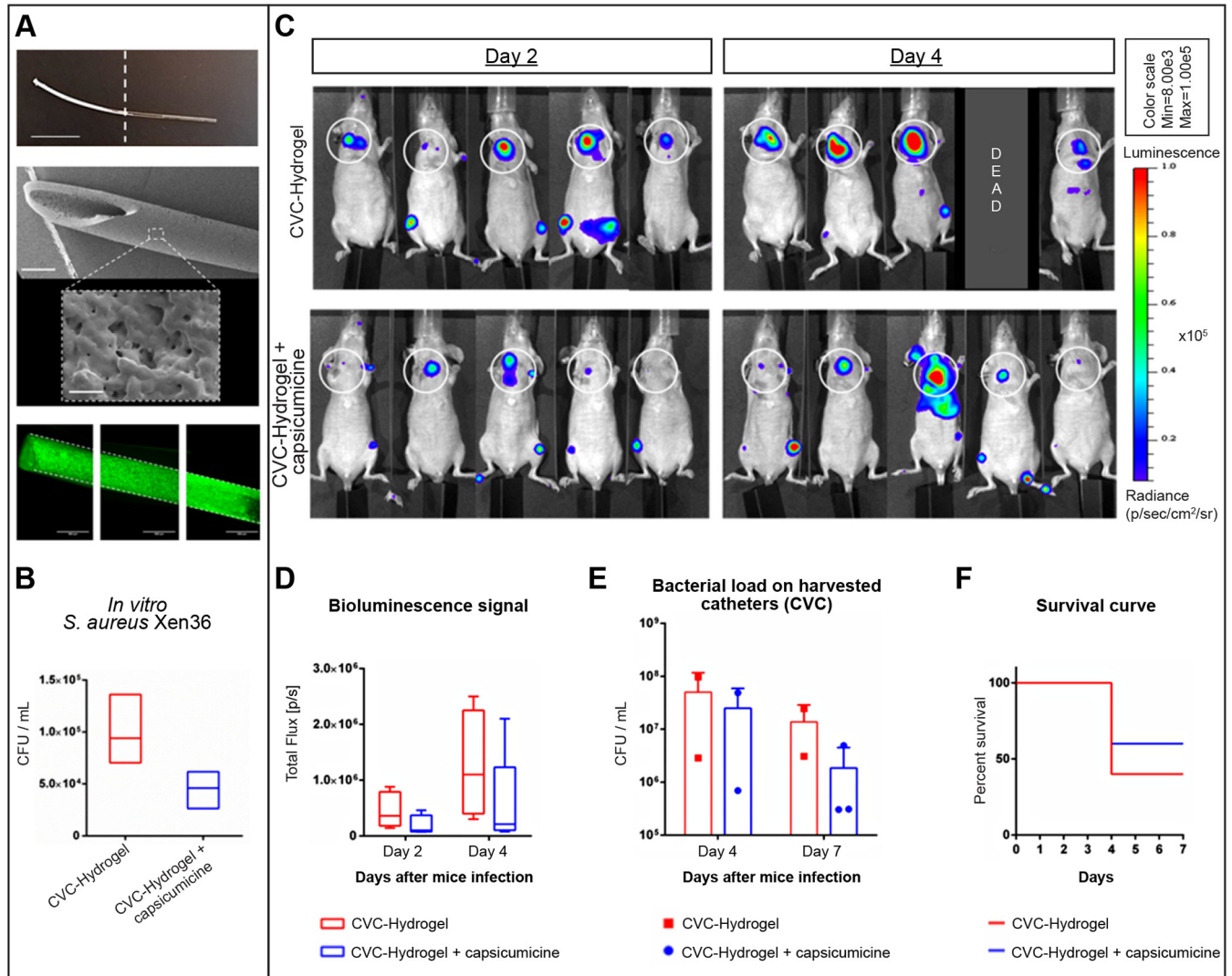


FIG 5 Assessment of capsicumine precoated central venous catheter (CVC) in mice (SKH1) infected by *Staphylococcus aureus* Xen36. (A and B) *In vitro* CVC development. (A) From the top to the bottom, a picture of up to half capsicumine precoated CVC (whitish) (scale bar, 1 cm), SEM image of precoated CVC (scale bar, 0.5 mm and its magnification scale bar, 1 μ m), and a compilation of images of fluorescence microscopy of precoated CVC (capsicumine-FITC in green). (B) Bacterial load on CVC. (C to F) *In vivo* CVC assessment. (C) IVIS images (radiance thresholded and smoothed with a bidimensional Gaussian filter) of ventral position for each mouse at each time point. The control group (CVC-hydrogel) is shown in the top and the treated (CVC-hydrogel + capsicumine) in the bottom. White circles delimitate the CVC localization, and the luminescence scale is presented in radiance. (D) Bioluminescence quantification (ROI mean signals \pm standard deviation [SD]) is shown as photons total flux (p/s) for each group at each time point. (E) Bacterial load (CFU/ml) on harvested CVC for each mouse at each time point (day 4 and 7 after infection). (F) The Kaplan-Meier survival curve (% of survival) at each group during the 7 days after infection. All bioluminescence data and analyses were performed using IVIS Spectrum of Perkin Elmer. All experiments were conducted in accordance with ethical committee and the French authorities ($n = 5$ /group). Bioluminescence images are presented with a defined pseudocolor scale to visualize the intensity of signals emitted.

immobilization polymer ("hydrogel") encompassing capsicumine. This coating confers amorphous and biocompatible surfaces to CVC (Fig. 5A). They were first validated *in vitro*, decreasing $\geq 51\%$ of *S. aureus* colonization (Fig. 5B). Then, bacterial development was evaluated *in vivo* by bioluminescence imaging and bacterial load of harvested CVC (Fig. 5C to F). Two days (D2) after *S. aureus* systemic infection, 40% of the control group (CVC-hydrogel) presented a high bioluminescence signal (red zones) related to region of interest (ROI) against none in the treated group (CVC-hydrogel + capsicumine) (Fig. 5C). Four days (D4) after infection, 75% of the control presented high ROI red zones against 20% in the treated group (Fig. 5C). In addition, at D4, 1 animal was found dead in the control group. Therefore, bioluminescence quantifications show that the treated group decreased 56% (D2) and 54% (D4) of the total flux compared to that of the control (Fig. 5D). This trend was also observed on the CFU load at

D4 (Fig. 5E). After image acquisitions (D4), 2 animals/group were euthanized due to ethical criteria. At the end of the experiment, 7 days after infection (D7), the treated group showed a decrease of 86% of bacterial load compared to that of the control (Fig. 5E). Macroscopic observation revealed that one animal from the control presented several organs with necrosis (liver, spleen, intestine, kidneys, and bladder). Finally, the treated group had an increased survival rate of 50% at D7 compared to that of the control (Fig. 5E).

DISCUSSION

Bioinspired peptides are increasingly being explored as alternative biofilm controls and have become important allies in the fight against bacterial tolerance and resistance (28, 29). As shown here, capsicumicine, a peptide derived from *Capsicum baccatum* red pepper seeds, possesses strong antibiofilm activity *in vitro* and *in vivo*. We demonstrated that capsicumicine strongly prevents biofilm formation for the most frequent bacteria related to nosocomial infections, *S. epidermidis* and *S. aureus*. However, all staphylococci do not produce a biofilm rich in polysaccharides, and considering the proposed mechanism of action of capsicumicine, this might be a limitation to our approach.

Capsicumicine prevents the establishment and maintenance of biofilm architecture through a mechanism of action that we named “matrix anti-assembly” (MAA). MAA differs from matrix disassembly (30), as instead of destructuring preestablished matrices, it acts on the initial phase of assembly preventing its correct structuration. In fact, established biofilms are harder to treat than initial biofilms because they have more complex structures (31), and increased structural complexity means that more energy is required for disassembly (32). Bacterial surface proteins can passively interact with surfaces such as medical devices, generating an initial and reversible adhesion after electrostatic and hydrophobic interactions, Van der Waals forces, and others (33). Bacteria will then require extracellular matrix production in order to remain attached after these weak interactions (34). During this process, physicochemical interactions drive molecular and colloidal matrix self-assembly, establishing a chain of dense architecture that results in stable adhesion (Fig. 6A) (35). In contrast, capsicumicine might interact with matrix saccharides and modify the self-assembly chain, resulting in a less dense and nonfunctional matrix and impaired biofilm formation (Fig. 6B). The capsicumicine amino acid sequence contains several residue characteristics for recognizing putative chitin-binding domains, including polar and hydrophobic residue (45% of Q) and cysteines (36–39). The chitin-binding domain is a well-conserved amino acid stretch that binds specifically to *N*-acetylglucosamine, a homologous structure of PIA (27, 40, 41). Additionally, noncatalytic carbohydrate-binding modules (CBMs) are contiguous amino acid sequences with a discreet fold displaying carbohydrate-binding activity. In this context, capsicumicine displays homologies with all tested CBM proteins, notably with the IcaA protein, which is a PIA synthetase from the same *S. epidermidis* strain studied here (see Fig. S3 and Table S2 in the supplemental material). According to the CAZY web site, there are currently 86 CBM families defined (<http://www.cazy.org/Carbohydrate-Binding-Modules.html>). CBMs exhibit different folds, with secondary structures ranging from mainly β -sheet-based organization to a mixture of α -helices and β -sheets, and usually display a high content of loops and unfolded parts. Likewise, the capsicumicine secondary fold is a mixture of α -helix, β -sheet, and unfolded regions, with conformational time and temperature interconversion in favor of β -sheet and unfolded segments. The β -sheet substructure observed in the CD concerns the Nter part of the peptide according to the chemical shifts of the corresponding amino acids (between 8.6 and 9.0). The TOCSY spectra analyses disclose that the conformational changes observed through time originate around the two cysteines, possibly involved in intermolecular disulfide bonds. This disulfide bond is possibly intermolecular since the formation of an intramolecular disulfide bond is only possible by bending the structure to get both cysteines close to each other. The size of different conformers

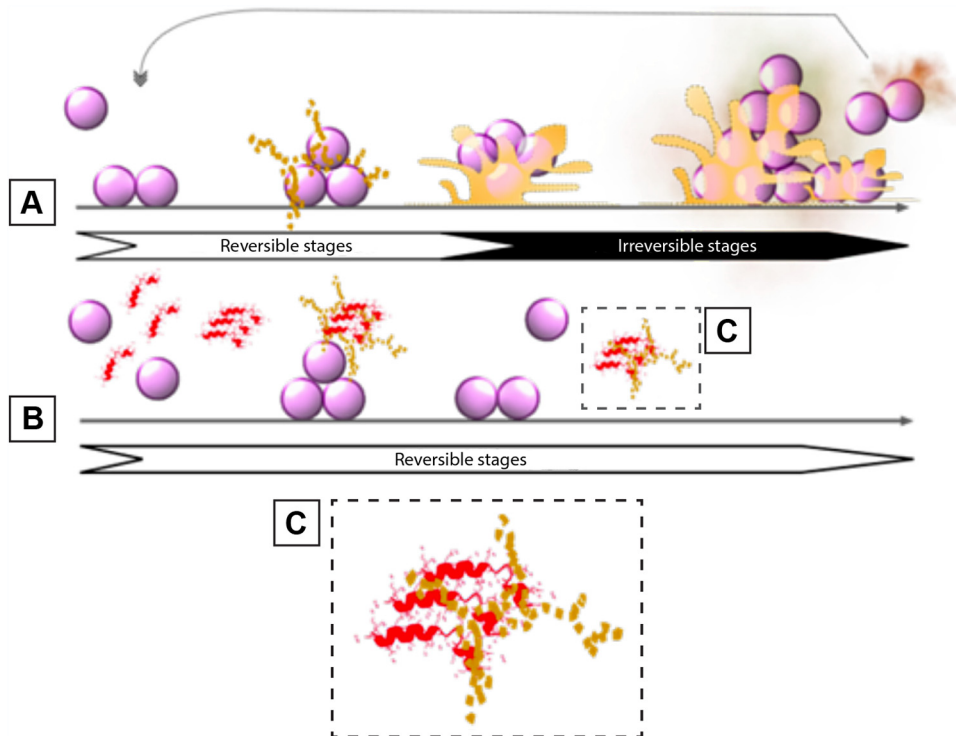


FIG 6 The matrix anti-assembly (MAA) antibiofilm mechanism of action identified in capsicumicine. (A) Untreated biofilm development on abiotic surfaces: planktonic cells interact passively with the surface and start the extracellular matrix production. Initial adhesion is established, after which matrix self-assembly occurs, leading to irreversible biofilm structuring and adhesion. (B) Biofilm development in the presence of capsicumicine shows the MAA mechanism of action: planktonic cells are still able to interact passively with the surface. At that point, capsicumicine acts, attracting extracellular saccharides and shifting the matrix self-assembly. (C) Capsicumicine (red) tends to organize itself in beta leaves favoring the interactions with matrix target-saccharides (yellow). These interactions occur between the noncatalytic carbohydrate-binding modules of the peptide and the saccharides. This peptide supra organization can compete with matrix assembly, preventing/destroying intramatrix H-bonds over a large range of residues. Consequently, the MAA decreases adhesion and aggregation, forcing bacteria to remain planktonic. The arrows indicate reversible (white background) and irreversible stages (black background) during biofilm formation.

and potential polymers are limited as shown by the NMR peaks of free peptides, which are not broadened at day 7 (Fig. 4C). As a result, these conformational changes may correspond to structural requirements for interactions with the staphylococcal matrix.

The proposed mechanism of action of capsicumicine matrix anti-assembly (MAA) is based on a set of intermolecular and cooperative forces that might be triggered by the peptide to disrupt matrix assembly.

Intermolecular forces. The staphylococcal matrix is composed mainly of polysaccharides but also contains proteins (AtIE, Aap, Empb), teichoic acids, and extracellular DNA (42). These saccharides are PIA/PNAG, homoglycans of beta-1,6-linked 2-amino-2-deoxy-D-glucopyranosyl residues. The matrix contains positively charged amino groups (PNAG) as well as negative charges from O-succinylation, which confers electrical charge lability on the matrix. Supported by NMR observations, capsicumicine interacts with free chitosan, a PNAG mimetic, and then switches to a higher-molecular-weight organization (Fig. 3B). The line broadening observed with the peptide-chitosan mixture after 1 day evidences the aggregation of chitosan particles with capsicumicine over time as schematized on Fig. 6. Likewise, CSP analysis reveals that chitosan is able to bind preferentially the capsicumicine N terminus (Fig. 4E) before intermolecular disulfide bridge formation and the relative conformational transition. This is supported by the fact that chitosan is substoichiometric at the end of the NMR titration and because the capsicumicine spectrum of the mixture is different from the spectra of the free peptide (Fig. 4C). These interactions may proceed by both hydrogen bonding between

the hydrophilic Q lateral chains and hydrophobic/stacking interactions involving I and L residues. According to NMR, the N-terminal part of the peptide is probably the favored interacting region with the carbohydrate moieties. Thus, these data support the MAA model, in which the peptide supra organization would compete with matrix self-assembly preventing intra h-bonds over a large range of residues. However, the NMR results obtained with assembled chitosan, mimicking a preformed biofilm, show that capsicumicine does not interact with the preassembled matrix (Fig. 3C and D), such as demonstrated in the eradication test. Additionally, the amino acids in capsicumicine are mostly neutral, counting 13 Q and 3 S, although due to the Q amide group and S hydroxyl group, they can generate electronegative (dipole-dipole) zones. This high electronegativity suggests that capsicumicine may interact with the positive free charges of the PIA/PNAG. Thus, these polar nonionic forces perform moderate interactions with the polysaccharides. Since strong interactions, such as ionic forces, may trigger unwanted effects including matrix repulsion or sequestration (43, 44), the moderate interactions of capsicumicine seem to be ideal.

Cooperative polymerization forces. In living systems, biomolecules perform their functions in the presence of various macromolecules of different shapes and sizes, and these interactions can include cooperative polymerization forces such as depletion forces (DFs) and subsequent molecular crowding (MC) (45, 46). These forces are noncovalent and nonspecific physicochemical interactions, leading to bridging, aggregation, and rheological variations (47, 48), as is observed in the presence of capsicumicine (Fig. 2D to G and Fig. 3A), and also may contribute to MAA. In a suspension containing different molecules, DFs are the pressures exerted by small particles, which in turn cause attractive forces between the macromolecules. DFs are only expressed in crowded environments like biofilms, driving the assembly and final shape of these structures (49). Taking together NMR and CD experimental results as well as the TANGO and SALSA analysis (see Fig. S5B in the supplemental material), we can picture that capsicumicine can self-organize to form extended structures both by disulfide bridges and β -sheet-mediated fibril formation. We propose that capsicumicine-associated DFs may coagulate in polymer solutions forming fibers and parallel bundles (50), explaining the observed branch-like profile (Fig. 2D to G) (51). This higher organization would facilitate the interaction with the saccharides of the matrix preventing their pattern assembly and resulting in flocculation (52). In the same way, MC in macromolecule solutions is characterized by a decrease in accessible volume due to high macromolecule concentrations, as well as attractive and repulsive forces between them (45, 53). Some molecular crowders modulate refolding kinetics and decrease competing aggregation and segregation (54). In this way, capsicumicine might enhance the aggregation kinetics (Fig. 3A), acting as an agent of MC, decreasing entropic forces, and leading to segregation (55). The *in vitro* interactions between capsicumicine and chitosan demonstrate that capsicumicine' structures are chemically able to interact with staphylococcal matrix saccharides. However, natural staphylococcal matrices are rather rich in PNAG and of course far more complex, making interactions with other matrix constituents also possible. These combined intermolecular and cooperative forces might disturb matrix self-assembly at both molecular and colloidal levels. Consequently, matrix functionality would shift and antibiofilm activity occur. Additionally, planktonic microorganisms are more available for the innate immune system to recognize and clear (56). Furthermore, nonantibiotic activity appears less susceptible to the development of bacteria resistance because these microorganisms are under less evolutionary pressure than when exposed to conventional antibiotics (57, 58).

Finally, although there are no antibiofilm drugs available yet, here, we relate the discovery of a new carbohydrate-binding peptide as a promising candidate for complementary drug/treatment of infectious diseases. In particular, we propose its antibiofilm mechanism of action, matrix anti-assembly (MAA), and validated a proof of concept for an *in vivo* application.

MATERIALS AND METHODS

Peptides. All peptides were synthesized by Biomatik and ProteoGenix at purity grades over 95% in salts suitable for cell culture. For the assays, the peptides were all solubilized in ultrapure sterile water.

Bacterial strains and growth conditions. *Staphylococcus epidermidis* ATCC 35984 was grown overnight on blood agar (Thermo Scientific Oxoid; PB5039A) at 37°C. Oxoid LB agar was used for the CFU assay. The other assays were done using a bacterial suspension of 3×10^8 CFU/ml in tryptone soya broth (TSB) (Oxoid) or 0.9% NaCl.

Biofilm formation. At least three technical and biological replicates were done for each assay of 1, 10, or 100 μ M peptide concentrations.

(i) Biofilm formation inhibition. A protocol adapted from Trentin et al. (59) was used with crystal violet (CV) in 96-well BD Falcon polyvinyl chloride (PVC) microtiter plates. The cell-bound stains were solubilized with absolute ethanol (Sigma-Aldrich), and absorbance was measured at 570 nm using a BioTek PowerWave XS plate reader. The biofilm formation control represents 100% of biofilm formation.

(ii) Biofilm eradication. Biofilm was preformed as described above for 24 h at 37°C without treatment. Afterwards, the wells were washed to remove planktonic cells, peptide solutions and controls were added, and all were incubated for 24 h. Biofilm eradication was verified by CV as previously described.

Bacterial growth assays. (i) Microtiter plates. Bacterial growth was evaluated by comparing OD₆₀₀ values at the start and end of incubation in 96-well PVC microtiter plates. After incubation at 37°C for 24 h, CFU per milliliter was calculated to determine the peptide solution's bactericidal effects. The untreated bacteria were considered as the growth control. At least three technical and biological replicates were performed for all assays.

(ii) Quantitative reverse transcription-PCR. After culturing for 24 h, RNAs were isolated from planktonic controls, biofilm controls, and from total cells exposed to 10 μ M capsiomicine. An Invitrogen TRIzol Max bacterial RNA isolation kit and an Ambion TURBO DNase treatment were used as per manufacturer instructions. Total RNA concentrations and purities were assessed using a Biochrom SimpliNano spectrophotometer, and PCRs were performed to ensure the complete absence of DNA. Each qRT-PCR was then subjected to previously established quantities of cDNA (10 ng) and primers (0.2 μ M). Reactional volumes and conditions were used as per the manufacturer's instructions (SYBR Select master mix; Applied Biosystems). Primers (see Table S1 in the supplemental material) were designed using the Primer3 program and then produced by Eurofins Genomics. Applied Biosystems StepOnePlus equipment and software were used. Relative transcript levels were determined by the $2^{-\Delta\Delta Ct}$ method (60).

(iii) Cytotoxicity assays. Cytotoxicity assays were performed on the ImPACcell robotic platform (BIOSIT, Université de Rennes 1). Multiparameter high-content screening (HCS) and high-content analysis (HCA) of chemical markers related to cell viability were done on 7 different mammalian lines as follows: HuH7 (hepatocellular carcinoma), Caco-2 (colorectal adenocarcinoma), MDA-MB231 (breast adenocarcinoma), HCT116 (colorectal carcinoma), PC3 (prostatic adenocarcinoma), NCL-H727 (lung carcinoma), and MCF7 (breast cancer). The number of viable cells is presented as residual cell percentage compared to the dimethyl sulfoxide (DMSO) control average.

Microscopic analysis. *S. epidermidis* ATCC 35984 biofilm was cultured as described above.

(i) Scanning electron microscopy. Sterile 10- by 4-mm polystyrene coupons were inserted into bacterial cultures in the presence or absence of capsiomicine for 1, 4, and 24 h. The coupons were then washed with sterile 0.9% NaCl and fixed with 2.5% glutaraldehyde, 2% paraformaldehyde, and 0.1 M cacodylate buffer (pH 7.2). Afterward, they were washed with 0.1 M cacodylate buffer and 0.2 M sucrose and then dehydrated with increasing concentrations of ethanol. A Leica EM CPD300 was used for critical point drying of the dehydrated samples. These were then sputtered with palladium in a Leica EM ACE200 and analyzed with a JEOL JSM-7100F microscope with energy-dispersive X-ray spectrometry (EDS) and electron backscatter diffraction (EBSD) at 10 kV.

(ii) Transmission electron microscopy. All well content was carefully detached at 1, 4, and 24 h, centrifuged at $10,000 \times g$ for 15 min at 4°C, and then washed with sterile 0.9% NaCl. Fixation was performed at 4°C with sodium 0.1 M cacodylate, 2% paraformaldehyde, 2.5% glutaraldehyde, and 75 mM lysine. Samples were washed with 0.1 M sodium cacodylate and 0.2 M sucrose and contrasted with 1% osmium tetroxide and 1.5% potassium ferrocyanide. Dehydration was done with a gradual solution of ethanol and infiltration of increasing concentrations of LR white resin (Delta Microscopies, France). LR white resin inclusion and polymerization were then performed over 24 h at 60°C in the absence of O₂. Thin 80-nm sections were collected onto carbon grids and visualized at 200 kV with an FEI Tecnai Sphera microscope equipped with a Gatan 4k x 4k charge-coupled device (CCD) UltraScan camera.

(iii) Confocal fluorescence microscopy. Capsiomicine-fluorescein isothiocyanate (capsiomicine-ITC) (10 μ M) was used to detect the capsiomicine peptide, whose antibiofilm activity was previously verified. After incubation for 1, 4, or 24 h, the well contents were carefully detached, centrifuged at $11,000 \times g$ for 2 min at 4°C, and then washed with sterile 0.9% NaCl. The suspension was visualized directly or after adding 0.1 μ g/ μ l concanavalin A conjugates (Alexa Fluor 633; Invitrogen) or 2 mg/ml Calcofluor white dye (Fluorescent Brightener 28; Sigma-Aldrich). The pseudonajide FITC-labeled peptide is a known antimicrobial peptide that permeates the bacterial cell and was used as a permeability reference (61). Images were acquired via resonant scanner with a Leica SP8 DMI 6000 CS confocal microscope with hybrid detector, and ImageJ software was used for image analysis.

Real-time molecular self-assembly assay. The assembly reaction of the synthetic staphylococcal matrix, starting at pH 7.2, was recorded by measuring the OD₆₀₀ as a function of time every 30 s for 30 min (35). Molecular self-assembly reactions were calculated to a final volume of 4 ml, with 0.3% chitosan (medium molecular weight, 75 to 85% deacetylation), 0.15% bovine serum albumin, and 0.015%

lambda DNA (all from Sigma) in TSB. The concentration (μM) of tested peptides was calculated for a final volume of 4 ml. Before getting the assembly reaction pH starting points, a calibration record was done using the same reactional tube containing all reagents (auto zero). Acetic acid and NaOH were used to adjust pH, and the reaction temperature was about 30°C. As a negative control, a similarly sized peptide was used, PA-1 (62).

NMR. NMR spectra were recorded in 3-mm tubes on a Bruker Avance III 600-MHz spectrometer equipped with a TXI (1H,13C,15N) probe and a Z-gradient unit. Spectra were processed with TopSpin 4.0.8 (Bruker Biospin) and CcpNmr analysis (63). TOCSY and NOESY experiments were respectively recorded at 10°C and pH 5.0 with a 70 ms and 300 ms mixing time. Capsicumicene concentration in water was set at 0.3 mM and the pH adjusted either to 5.0 or to 3.5 with a few microliters of deuterated HCl 0.1 M and/or NaOH 0.1 M solutions. Chitosan powder (purchased from Sigma) was dissolved in pure water and the pH adjusted to either 5.0 or 3.5. Reference 1D proton NMR spectra were recorded at 10°C and either at pH 3.5 and 5.0. Chitosan was stepwise added from a concentrated solution at pH 5.0 or 3.5, and spectra changes were monitored. We first titrated capsicumicene solution with chitosan solution at pH 5.0. The concentration variation of chitosan was estimated using the peaks intensities, resulting in 3.6 and 3.8 ppm (not shown) in the beginning to less than 0.5 eq at the end of the titration. These experiments were repeated with a starting capsicumicene solution at pH 3.5 and the gradual addition of gelled chitosan at pH 3.5 and the sudden addition of gelled chitosan pellets in the NMR solution at pH 3.5.

Circular dichroism. The peptide was dissolved in 18 M Ω water at a concentration of 50 μM at pH 5.0. The UV CD spectra were recorded at 5, 15, and 30°C in a 0.1-cm path length quartz cell on a Jobin Yvon CD6 spectrometer equipped with a temperature controller unit over a 180- to 260-nm range with a 2-nm bandwidth, a step size of 1 nm, and an integration time of 2 s per point. The samples were conserved at 5°C between each recording. Spectra were averaged over 5 records. Water CD contributions were subtracted from CD spectra before processing. Spectra were processed using KaleidaGraph (Synergy Software). Molar circular dichroism ($\Delta\epsilon$) per residue and molar ellipticity per residue (θ) (MER) were computed from the difference of the delta absorbance recorded by the spectrometer. Raw delta epsilon per residue spectra were analyzed using the CDSSTR program (64) and different reference protein data sets provided by the DICHROWEB facility (65). MER data curves were smoothed for presentation, using the interpolate and weighted data (5%) routines provide by KaleidaGraph.

TANGO and SALSA predictions. Tango (66) and Salsa (67) predictions were run using the AMYPdb online web server (http://amypdb.genouest.org/e107_plugins/amypdb_project/project.php) (68). For Tango temperature was set to 298 K. Predictions were both run with pH set either to 5.0, 7.0, or 9.0. SALSA predictions were run with a window size dynamic 512 of 4 to 20 residues, a cutoff of 1.2, and a minimal hot spot length of 5.

CVC coatings. We adapted an approach to immobilize peptides based on poly(ethylene glycol)diacrylate (PEGDA) hydrogel (69). Briefly, polyurethane (PU) tubes (Instech) of 2 Fr or 25 G equivalent (0.4 to 0.7 mm of diameter) were used as coating framework. Hydrogel base was prepared using pentaerythritol tetrakis(3-mercaptopropionate) (PTMP) (4.1 mmol), PEGDA (10 mmol), PEG-600 (20 mM), 2,2-dimethoxy-2-phenylacetophenone (DMPA) (0.1 wt%), THF soluble PU (10 wt%), and methanol (qs). Peptides were solubilized in DMSO and added to a hydrogel base under vortex agitation. PU tubes were first internally coated by suction using a needle syringe and then externally by immersion. The reaction and polymerization conditions such as room temperature and oxygen tolerance were easily implemented. After polymerization, successive washes with methanol under agitation were used to eliminate undesirable monomers. All reagents were purchased from Sigma-Aldrich.

CVC infection assay. This study was conducted by Voxcan s.a.r.l. The ethical agreement is part of project APAFIS number 10756-2017072522272676 v4, approved by the Voxcan ethical committee (CEAA-129) and the French authorities (Ministry of National Education, the Higher Education and Research). This study used *S. aureus* rather than *S. epidermidis* for the *in vivo* experiment because of the poor bioluminescent activity of the known *S. epidermidis* strain. Indeed, the previously described bioluminescent *S. epidermidis* strain is no longer available, as its light-emission levels are not stable (see Fig. S1 in reference 70). Since the use of bioluminescence for quantifying bacterial colonization and biofilm formation significantly reduces the number of animals needed for testing, thus decreasing the need for euthanasia at each point/time in the analysis, we decided to base the study on bioluminescent *S. aureus*. We therefore first validated the *in vitro* activity of capsicumicene with the bioluminescent *S. aureus* (see Fig. 5b). This study used SKH1 mice, females, immunocompetent, and specific pathogen free (SPF) provided by Charles River Laboratories. Animals were acclimated at least 2 days, housed collectively in disposable standard cages in ventilated racks A3 biological safety, at $+21 \pm 3^\circ\text{C}$, 30 to 70% humidity, and 12-h dark and light cycles, with filtered water and autoclaved standard food provided *ad libitum*. Catheters were blind implanted ($n = 5/\text{group}$) in mice jugular vein followed by an intravenous (i.v.) inoculation of *S. aureus* Xen36 5 days later, which was in turn to colonize the device from blood circulation. The bacterial development was evaluated and compared between the different catheters by *in vivo* bioluminescence imaging (IVIS Spectrum; acquisition and analysis with Living Image version 4.5.5) performed 2 and 4 days after mice infection. In addition, 7 days after inoculation or at the time of mice euthanasia for ethical reason, catheters were harvested and bacterial load was evaluated by CFU counting (SCAN500). All along the study, mice clinical state was evaluated using a scoring grid and body weight measurements 3 times a week. At each time point, a bioluminescence acquisition was also performed on the background (BKG) mouse to measure the flux level corresponding to the autoluminescence. Images were radiance-thresholded with respect to the background radiance level and smoothed with a bidimensional Gaussian filter (3 by 3).

Data availability. All data needed to evaluate the conclusions in this article are present in the paper and/or the Supplemental Material. Additional data related to this paper may be requested from the authors.

SUPPLEMENTAL MATERIAL

Supplemental material is available online only.

SUPPLEMENTAL FILE 1, PDF file, 2.5 MB.

ACKNOWLEDGMENTS

We thank Daniel Thomas for his support and Juliana Berland for insightful comments on the manuscript.

We thank the Microscopy Rennes Imaging Center (MRic) and CMEBA facilities.

This study was funded by the CAPES-COFEUCUB program, whose institutional partners are the Brazilian Ministry of Education's CAPES (Coordenação de Aperfeiçoamento de Pessoal de Nível Superior) agency and the French Ministère de l'Europe et des Affaires Étrangères (MEAE) and Ministère de l'Enseignement supérieur, de la Recherche et de l'Innovation (MESRI). Support was also received from the Transfer Acceleration Company SATT Ouest-Valorisation.

R.G.V.B., S.C.B.G., A.J.M., S.N-L., and R.G. designed the research; R.G.V.B., S.C., R.S., S.N-L., and S.B. performed research; R.G.V.B., A.R.Z., E.G., S.C.B.G., A.J.M., S.N-L., S.B., and R.G. analyzed data; and R.G.V.B., A.J.M., S.N-L., and R.G. wrote the paper.

R.G.V.B., S.C.B.G., A.R.Z., A.J.M., and R.G. are co-authors of a patent register of capsicumicine. Application number WO 2020/169709 A1 at European Patent Office. Specific aspects of this article are covered in the patent application (its amino acid sequence and bioactivity).

REFERENCES

- World Health Organization. 2015. WHO Library Cataloguing-in-Publication data. Global action plan on antimicrobial resistance. I. World Health Organization, Geneva, Switzerland.
- World Health Organization. 2018. WHO competency framework for health workers' education and training on antimicrobial resistance. World Health Organization, Geneva, Switzerland. <https://www.who.int/hrh/resources/WHO-HIS-HWF-AMR-2018.1/en>. Accessed 12 January 2019.
- Penesyan A, Gillings M, Paulsen IT. 2015. Antibiotic discovery: combatting bacterial resistance in cells and in biofilm communities. *Molecules* 20: 5286–5298. <https://doi.org/10.3390/molecules20045286>.
- Flemming H-C, Wingender J. 2010. The biofilm matrix. *Nat Rev Microbiol* 8:623–633. <https://doi.org/10.1038/nrmicro2415>.
- Taglialegna A, Navarro S, Ventura S, Garnett JA, Matthews S, Penades JR, Lasa I, Valle J. 2016. Staphylococcal Bap proteins build amyloid scaffold biofilm matrices in response to environmental signals. *PLoS Pathog* 12: e1005711. <https://doi.org/10.1371/journal.ppat.1005711>.
- Hoiby N, Bjarnsholt T, Givskov M, Molin S, Ciofu O. 2010. Antibiotic resistance of bacterial biofilms. *Int J Antimicrob Agents* 35:322–332. <https://doi.org/10.1016/j.ijantimicag.2009.12.011>.
- Beloin C, Renard S, Ghigo JM, Lebeaux D. 2014. Novel approaches to combat bacterial biofilms. *Curr Opin Pharmacol* 18:61–68. <https://doi.org/10.1016/j.coph.2014.09.005>.
- Davies D. 2003. Understanding biofilm resistance to antibacterial agents. *Nat Rev Drug Discov* 2:114–122. <https://doi.org/10.1038/nrd1008>.
- Brauner A, Fridman O, Gefen O, Balaban NQ. 2016. Distinguishing between resistance, tolerance and persistence to antibiotic treatment. *Nat Rev Microbiol* 14:320–330. <https://doi.org/10.1038/nrmicro.2016.34>.
- Defraigne V, Fauvart M, Michiels J. 2018. Fighting bacterial persistence: current and emerging anti-persister strategies and therapeutics. *Drug Resist Updat* 38:12–26. <https://doi.org/10.1016/j.drug.2018.03.002>.
- Otto M. 2014. Physical stress and bacterial colonization. *FEMS Microbiol Rev* 38:1250–1270. <https://doi.org/10.1111/1574-6976.12088>.
- Uçkay I, Harbarth S, Ferry T, Lübbecke A, Emonet S, Hoffmeyer P, Pittet D. 2011. Meticillin resistance in orthopaedic coagulase-negative staphylococcal infections. *J Hosp Infect* 79:248–253. <https://doi.org/10.1016/j.jhin.2011.06.014>.
- Otto M. 2008. Staphylococcal biofilms. *Curr Top Microbiol Immunol* 322: 207–228. https://doi.org/10.1007/978-3-540-75418-3_10.
- Nishizaki Y, Yamagami S, Joki Y, Takahashi S, Sesoko M, Yamashita H, Yokoyama T, Uehara Y, Daida H. 2013. Japanese features of native valve endocarditis caused by coagulase-negative staphylococci: case reports and a literature review. *Intern Med* 52:567–572. <https://doi.org/10.2169/internalmedicine.52.9017>.
- Abad CL, Haleem A. 2018. Prosthetic joint infections: an update. *Curr Infect Dis Rep* 20:15. <https://doi.org/10.1007/s11908-018-0622-0>.
- Rupp ME. 2014. Clinical characteristics of infections in humans due to *Staphylococcus epidermidis*. *Methods Mol Biol* 1106:1–16. https://doi.org/10.1007/978-1-62703-736-5_1.
- Center for Disease Control and Prevention. 2011. Vital signs: central line-associated blood stream infections—United States, 2001, 2008, and 2009. *MMWR Morb Mortal Wkly Rep* 60:243–248.
- Lee JYH, Monk IR, Gonçalves da Silva A, Seemann T, Chua KYL, Kearns A, Hill R, Woodford N, Bartels MD, Strommenger B, Laurent F, Dodémont M, Deplano A, Patel R, Larsen AR, Korman TM, Stinear TP, Howden BP. 2018. Global spread of three multidrug-resistant lineages of *Staphylococcus epidermidis*. *Nat Microbiol* 3:1175–1185. <https://doi.org/10.1038/s41564-018-0230-7>.
- Streit JM, Jones RN, Sader HS, Fritsche TR. 2004. Assessment of pathogen occurrences and resistance profiles among infected patients in the intensive care unit: report from the SENTRY Antimicrobial Surveillance Program (North America, 2001). *Int J Antimicrob Agents* 24:111–118. <https://doi.org/10.1016/j.ijantimicag.2003.12.019>.
- Flamm RK, Mendes RE, Hogan PA, Streit JM, Ross JE, Jones RN. 2016. Linezolid surveillance results for the United States (LEADER surveillance program 2014). *Antimicrob Agents Chemother* 60:2273–2280. <https://doi.org/10.1128/AAC.02803-15>.
- Hope R, Livermore DM, Brick G, Lillie M, Reynolds R, BSAC Working Parties on Resistance Surveillance. 2008. Non-susceptibility trends among staphylococci from bacteraemias in the UK and Ireland, 2001–06. *J Antimicrob Chemother* 62(Suppl 2):65–74. <https://doi.org/10.1093/jac/dkn353>.
- Stempel N, Strehmel J, Overhage J. 2015. Potential application of antimicrobial peptides in the treatment of bacterial biofilm infections. *Curr Pharm Des* 21:67–84. <https://doi.org/10.2174/1381612820666140905124312>.

23. de la Fuente-Nunez C, Reffuveille F, Mansour SC, Reckseidler-Zenteno SL, Hernández D, Brackman G, Coenye T, Hancock REW. 2015. D-enantiomeric peptides that eradicate wild-type and multidrug-resistant biofilms and protect against lethal *Pseudomonas aeruginosa* infections. *Chem Biol* 22:196–205. <https://doi.org/10.1016/j.chembiol.2015.01.002>.
24. El-Halfawy OM, Czarny TL, Flannagan RS, Day J, Bozelli JC, Kuiack RC, Salim A, Eckert P, Epanand RM, McGavin MJ, Organ MG, Heinrichs DE, Brown ED. 2020. Discovery of an antivirulence compound that reverses β -lactam resistance in MRSA. *Nat Chem Biol* 16:143–149. <https://doi.org/10.1038/s41589-019-0401-8>.
25. Borowski RG, Barros MP, da Silva DB, Lopes NP, Zimmer KR, Staats CC, de Oliveira CB, Giudice E, Gillet R, Macedo AJ, Gnoatto SCB, Zimmer AR. 2020. Red pepper peptide coatings control *Staphylococcus epidermidis* adhesion and biofilm formation. *Int J Pharm* 574:118872. <https://doi.org/10.1016/j.ijpharm.2019.118872>.
26. The UniProt Consortium. 2017. UniProt: the universal protein knowledgebase. *Nucleic Acids Res* 45:D158–D169. <https://doi.org/10.1093/nar/gkw1099>.
27. Lombard V, Golaconda Ramulu H, Drula E, Coutinho PM, Henrissat B. 2014. The carbohydrate-active enzymes database (CAZY) in 2013. *Nucleic Acids Res* 42:D490–D495. <https://doi.org/10.1093/nar/gkt1178>.
28. Feuillie C, Formosa-Dague C, Hays LMC, Vervaeck O, Derclaye S, Brennan MP, Foster TJ, Geoghegan JA, Dufrière YF. 2017. Molecular interactions and inhibition of the staphylococcal biofilm-forming protein SdrC. *Proc Natl Acad Sci U S A* 114:3738–3743. <https://doi.org/10.1073/pnas.1616805114>.
29. Schmitt S, Montalbán-López M, Peterhoff D, Deng J, Wagner R, Held M, Kuipers OP, Panke S. 2019. Analysis of modular bioengineered antimicrobial lanthipeptides at nanoliter scale. *Nat Chem Biol* 15:437–443. <https://doi.org/10.1038/s41589-019-0250-5>.
30. Roy R, Tiwari M, Donelli G, Tiwari V. 2018. Strategies for combating bacterial biofilms: a focus on anti-biofilm agents and their mechanisms of action. *Virulence* 9:522–554. <https://doi.org/10.1080/21505594.2017.1313372>.
31. Jabbouri S, Sadovskaya I. 2010. Characteristics of the biofilm matrix and its role as a possible target for the detection and eradication of *Staphylococcus epidermidis* associated with medical implant infections. *FEMS Immunol Med Microbiol* 59:280–291. <https://doi.org/10.1111/j.1574-695X.2010.00695.x>.
32. Fleming D, Rumbaugh KP. 2017. Approaches to dispersing medical biofilms. *Microorganisms* 5:15. <https://doi.org/10.3390/microorganisms5020015>.
33. Armbruster CR, Parsek MR. 2018. New insight into the early stages of biofilm formation. *Proc Natl Acad Sci U S A* 115:4317–4319. <https://doi.org/10.1073/pnas.1804084115>.
34. Otto M. 2013. Staphylococcal infections: mechanisms of biofilm maturation and detachment as critical determinants of pathogenicity. *Annu Rev Med* 64:175–188. <https://doi.org/10.1146/annurev-med-042711-140023>.
35. Stewart EJ, Ganesan M, Younger JG, Solomon MJ. 2015. Artificial biofilms establish the role of matrix interactions in staphylococcal biofilm assembly and disassembly. *Sci Rep* 5:13081. <https://doi.org/10.1038/srep13081>.
36. Hemmi H, Ishibashi J, Tomie T, Yamakawa M. 2003. Structural basis for new pattern of conserved amino acid residues related to chitin-binding in the antifungal peptide from the coconut rhinoceros beetle *Oryctes rhinoceros*. *J Biol Chem* 278:22820–22827. <https://doi.org/10.1074/jbc.M301025200>.
37. Suetake T, Tsuda S, Kawabata S, Miura K, Iwanaga S, Hikichi K, Nitta K, Kawano K. 2000. Chitin-binding proteins in invertebrates and plants comprise a common chitin-binding structural motif. *J Biol Chem* 275:17929–17932. <https://doi.org/10.1074/jbc.C000184200>.
38. Wright HT, Sandrasegaram G, Wright CS. 1991. Evolution of a family of N-acetylglucosamine binding proteins containing the disulfide-rich domain of wheat germ agglutinin. *J Mol Evol* 33:283–294. <https://doi.org/10.1007/BF02100680>.
39. Yin J, Yang S, Li K, Guo W, Cao Y. 2014. Identification and molecular characterization of a chitin-binding protein from the beet webworm, *Loxostege sticticalis* L. *Int J Mol Sci* 15:19147–19161. <https://doi.org/10.3390/ijms151019147>.
40. El-Gebali S, Mistry J, Bateman A, Eddy SR, Luciani A, Potter SC, Qureshi M, Richardson LJ, Salazar GA, Smart A, Sonnhammer ELL, Hirsh L, Paladin L, Piovesan D, Tosatto SCE, Finn RD. 2019. The Pfam protein families database in 2019. *Nucleic Acids Res* 47:D427–D432. <https://doi.org/10.1093/nar/gky995>.
41. Suginta W, Sirimontree P, Sritho N, Ohnuma T, Fukamizo T. 2016. The chitin-binding domain of a GH-18 chitinase from *Vibrio harveyi* is crucial for chitin-chitinase interactions. *Int J Biol Macromol* 93:1111–1117. <https://doi.org/10.1016/j.ijbiomac.2016.09.066>.
42. Paharik AE, Horswill AR. 2016. The staphylococcal biofilm: adhesins, regulation, and host response. *Microbiol Spectr* 4:4.2.06. <https://doi.org/10.1128/microbiolspec.VMBF-0022-2015>.
43. Batoni G, Maisetta G, Esin S. 2016. Antimicrobial peptides and their interaction with biofilms of medically relevant bacteria. *Biochim Biophys Acta* 1858:1044–1060. <https://doi.org/10.1016/j.bbammem.2015.10.013>.
44. Sharma A, Gupta P, Kumar R, Bhardwaj A. 2016. dPABs: a novel in silico approach for predicting and designing anti-biofilm peptides. *Sci Rep* 6: 21839. <https://doi.org/10.1038/srep21839>.
45. Banani SF, Lee HO, Hyman AA, Rosen MK. 2017. Biomolecular condensates: organizers of cellular biochemistry. *Nat Rev Mol Cell Biol* 18: 285–298. <https://doi.org/10.1038/nrm.2017.7>.
46. Rest C, Kandanelli R, Fernández G. 2015. Strategies to create hierarchical self-assembled structures via cooperative non-covalent interactions. *Chem Soc Rev* 44:2543–2572. <https://doi.org/10.1039/C4CS00497C>.
47. Kudlay A, Cheung MS, Thirumalai D. 2012. Influence of the shape of crowding particles on the structural transitions in a polymer. *J Phys Chem B* 116:8513–8522. <https://doi.org/10.1021/jp212535n>.
48. Even C, Marlière C, Ghigo J-M, Allain J-M, Marcellan A, Raspaud E. 2017. Recent advances in studying single bacteria and biofilm mechanics. *Adv Colloid Interface Sci* 247:573–588. <https://doi.org/10.1016/j.cis.2017.07.026>.
49. Marenduzzo D, Finan K, Cook PR. 2006. The depletion attraction: an underappreciated force driving cellular organization. *J Cell Biol* 175: 681–686. <https://doi.org/10.1083/jcb.200609066>.
50. Zhou HX. 2008. Effect of mixed macromolecular crowding agents on protein folding. *Proteins* 72:1109–1113. <https://doi.org/10.1002/prot.22111>.
51. Sakaguchi A, Higashiguchi K, Matsuda K. 2018. Bundle formation of supramolecular fibers of amphiphilic diarylethene by depletion force. *Chem Commun (Camb)* 54:4298–4301. <https://doi.org/10.1039/c8cc01666f>.
52. Fantoni R, Santos A. 2014. Depletion force in the infinite-dilution limit in a solvent of nonadditive hard spheres. *J Chem Phys* 140:244513. <https://doi.org/10.1063/1.4884353>.
53. Aumiller WM, Davis BW, Keating CD. 2014. Phase separation as a possible means of nuclear compartmentalization. *Int Rev Cell Mol Biol* 307: 109–149. <https://doi.org/10.1016/B978-0-12-800046-5.00005-9>.
54. Biswas S, Kundu J, Mukherjee SK, Chowdhury PK. 2018. Mixed macromolecular crowding: a protein and solvent perspective. *ACS Omega* 3: 4316–4330. <https://doi.org/10.1021/acsomega.7b01864>.
55. Polson JM, Kerry DR. 2018. Segregation of polymers under cylindrical confinement: effects of polymer topology and crowding. *Soft Matter* 14: 6360–6373. <https://doi.org/10.1039/c8sm01062e>.
56. de la Fuente-Núñez C, Reffuveille F, Fernández L, Hancock RE. 2013. Bacterial biofilm development as a multicellular adaptation: antibiotic resistance and new therapeutic strategies. *Curr Opin Microbiol* 16:580–589. <https://doi.org/10.1016/j.mib.2013.06.013>.
57. Krachler AM, Orth K. 2013. Targeting the bacteria-host interface: strategies in anti-adhesion therapy. *Virulence* 4:284–294. <https://doi.org/10.4161/viru.24606>.
58. Travier L, Rendueles O, Ferrieres L, Herry J-M, Ghigo J-M. 2013. *Escherichia coli* resistance to nonbiocidal antibiofilm polysaccharides is rare and mediated by multiple mutations leading to surface physicochemical modifications. *Antimicrob Agents Chemother* 57:3960–3968. <https://doi.org/10.1128/AAC.02606-12>.
59. Trentin DDS, Giordani RB, Zimmer KR, da Silva AG, da Silva MV, Correia MTDS, Baumvol IJR, Macedo AJ. 2011. Potential of medicinal plants from the Brazilian semi-arid region (Caatinga) against *Staphylococcus epidermidis* planktonic and biofilm lifestyles. *J Ethnopharmacol* 137:327–335. <https://doi.org/10.1016/j.jep.2011.05.030>.
60. Livak KJ, Schmittgen TD. 2001. Analysis of relative gene expression data using real-time quantitative PCR and the 2⁻(Delta Delta C(T)) method. *Methods* 25:402–408. <https://doi.org/10.1006/meth.2001.1262>.
61. Schneider R, Primon-Barros M, Von Borowski RG, Chat S, Nonin-Lecomte S, Gillet R, Macedo AJ. 2020. Pseudonajide peptide derived from snake venom alters cell envelope integrity interfering on biofilm formation in *Staphylococcus epidermidis*. *BMC Microbiol* 20:237. <https://doi.org/10.1186/s12866-020-01921-5>.
62. Liu P, Huang D, Hu X, Tang Y, Ma X, Yan R, Han Q, Guo J, Zhang Y, Sun Q, Liu Z. 2017. Targeting inhibition of SmpB by peptide aptamer attenuates the virulence to protect zebrafish against *Aeromonas veronii* infection. *Front Microbiol* 8:1766. <https://doi.org/10.3389/fmicb.2017.01766>.
63. Skinner SP, Fogh RH, Boucher W, Ragan TJ, Mureddu LG, Vuister GW. 2016. CcpNmr AnalysisAssign: a flexible platform for integrated NMR analysis. *J Biomol NMR* 66:111–124. <https://doi.org/10.1007/s10858-016-0060-y>.

64. Sreerama N, Woody RW. 2000. Estimation of protein secondary structure from circular dichroism spectra: comparison of CONTIN, SELCON, and CDSSTR methods with an expanded reference set. *Anal Biochem* 287: 252–260. <https://doi.org/10.1006/abio.2000.4880>.
65. Whitmore L, Wallace BA. 2004. DICHROWEB, an online server for protein secondary structure analyses from circular dichroism spectroscopic data. *Nucleic Acids Res* 32:W668–W673. <https://doi.org/10.1093/nar/gkh371>.
66. Fernandez-Escamilla AM, Rousseau F, Schymkowitz J, Serrano L. 2004. Prediction of sequence-dependent and mutational effects on the aggregation of peptides and proteins. *Nat Biotechnol* 22:1302–1306. <https://doi.org/10.1038/nbt1012>.
67. Zibae S, Makin OS, Goedert M, Serpell LC. 2007. A simple algorithm locates beta-strands in the amyloid fibril core of alpha-synuclein, Abeta, and tau using the amino acid sequence alone. *Protein Sci* 16:906–918. <https://doi.org/10.1110/ps.062624507>.
68. Pawlicki S, Le Behec A, Delamarche C. 2008. AMYPdb: a database dedicated to amyloid precursor proteins. *BMC Bioinformatics* 9:273. <https://doi.org/10.1186/1471-2105-9-273>.
69. Cleophas RTC, Riool M, Quarles van Ufford HLC, Zaat SAJ, Kruijtz JAW, Liskamp RMJ. 2014. Convenient preparation of bactericidal hydrogels by covalent attachment of stabilized antimicrobial peptides using thiol–ene click chemistry. *ACS Macro Lett* 3:477–480. <https://doi.org/10.1021/mz5001465>.
70. Chauhan A, Lebeaux D, Decante B, Kriegel I, Escande MC, Ghigo JM, Beloin C. 2012. A rat model of central venous catheter to study establishment of long-term bacterial biofilm and related acute and chronic infections. *PLoS One* 7:e37281. <https://doi.org/10.1371/journal.pone.0037281>.